Assessment of dynamic characteristics of fluidized beds via numerical simulations

Feichi Zhang (张飞驰) ✉ 📷 ; Salar Tavakkol; Stefan Dercho; Jialing Zhou (周佳铃); Thorsten Zirwes 📷 ; Michael Zeller 📷 ; Jonas Vogt 📷 ; Rui Zhang (张睿); Henning Bockhorn 📷 ; Dieter Stapf 📷

Check for updates

View Online   Export Citation   CrossMark

Physics of Fluids

Special Topic: Overview of Fundamental and Applied Research in Fluid Dynamics in UK

Submit Today

AIP Publishing

Assessment of dynamic characteristics of fluidized beds via numerical simulations

View Online   Export Citation   CrossMark

Feichi Zhang (张飞驰),[1,a] (iD) Salar Tavakkol,[1] Stefan Dercho,[1] Jialing Zhou (周佳铃),[2] Thorsten Zirwes,[3] (iD)
Michael Zeller,[1] (iD) Jonas Vogt,[1] (iD) Rui Zhang (张睿),[2] Henning Bockhorn,[4] (iD) and Dieter Stapf[1] (iD)

AFFILIATIONS

[1]Institute for Technical Chemistry, Karlsruhe Institute of Technology, Kaiserstr. 12, 76131 Karlsruhe, Germany
[2]Nanjing University of Science and Technology, Xiaolingwei Street, 210094 Nanjing, China
[3]Institute for Combustion Technology, University of Stuttgart, Pfaffenwaldring 31, 70569 Stuttgart, Germany
[4]Engler-Bunte-Institute, Division of Combustion Technology, Karlsruhe Institute of Technology,
  Engler-Bunte-Ring 1, 76131 Karlsruhe, Germany

[a]Author to whom correspondence should be addressed: feichi.zhang@kit.edu

ABSTRACT

Euler–Lagrange simulations coupled with the multiphase particle-in-cell (MP-PIC) approach for considering inter-particulate collisions have been performed to simulate a non-reacting fluidized bed at laboratory-scale. The objective of this work is to assess dynamic properties of the fluidized bed in terms of the specific kinetic energy of the bed material k_S in J/kg and the bubble frequency f_B in Hz, which represent suitable measures for the efficiency of the multiphase momentum exchange and the characteristic timescale of the fluidized bed system. The simulations have reproduced the bubbling fluidization regime observed in the experiments, and the calculated pressure drop Δp in Pa has shown a reasonably good agreement with measured data. While varying the bed inventory m_S in kg and the superficial gas velocity u_G in m/s, k_S increases with u_G due to the increased momentum of the gas flow, which leads to a reinforced gas-to-solid momentum transfer. In contrast, f_B decreases with m_S, which is attributed to the increased bed height h_B in m at larger m_S. An increased gas temperature T_G from 20 to 500 °C has led to an increase in k_S by approximately 50%, whereas Δp, h_B, and f_B are not sensitive to T_G. This is due to the increased gas viscosity with T_G, which results in an increased drag force exerted by the gas on the solid phase. While up-scaling the reactor to increase the bed inventory, bubble formation is enhanced significantly. This has led to an increased f_B, whereas k_S, h_B, and Δp remain almost unchanged during the scale-up process. The results reveal that the general parameters such as h_B and Δp are not sufficient for assessing the hydrodynamic behavior of a fluidized bed while varying the operating temperatures and up-scaling the reactor dimension. In these cases, the dynamic properties k_S and f_B can be used as more suitable parameters for characterizing the hydrodynamics of fluidized beds.

I. INTRODUCTION

Gas–solid fluidized beds are characterized by a large gas–solid contact surface and an intensive gas–solid mixing, which promote heat and mass transfer. Due to these advantages, the fluidized bed technology is widely employed to environmental, chemical, pharmaceutical, energy and process industries, which can benefit significantly to higher efficiencies and lower emissions of these processes. For example, fluidized beds are used as a key technology in the petroleum refining industry (fluid catalytic cracking), drying of powder and granules, reduction of iron ore, biomass/coal combustion, and gasification.[1–3] The operational performance of fluidized beds relies strongly on the hydrodynamics of the gas–solid flow in terms of bubble formation and particle

dynamics, which represent the fundamental mechanism for the mass and heat transfer, and also influence the product yield. As the harsh environment caused by the dense particulate flow limits the experimental assessment of the gas–solid flow system within the fluidized bed, numerical simulations have been used extensively in the last few decades to gain an in-depth understanding of the underlying fluidization dynamics.

There are two fundamental approaches for modeling gas–solid flows: the Euler–Euler and the Euler–Lagrange approach.[4] The two-fluid model (TFM) uses the Euler–Euler approach, and both gas and solid are regarded as penetrating continuous phases. Therewith, the particle properties such as density or diameter are calculated using the

kinetic theory of granular flow (KTGF).[5] The TFM is widely used due to its low computational cost. However, the effect of particle size cannot be considered properly by TFM, which can have significant influence on prediction performance of fluidized beds.[6] In the Euler–Lagrange method, a large number of Lagrange particles (LPs) are tracked, which interact with the continuous gas phase. Both phases are coupled through source terms concerning mass, momentum, and heat transfer. Compared with TFM, the Euler–Lagrange approach takes the effect of particle size distribution (PSD) into account[7] and it provides information on the trajectories as well as transient forces acting on the particles.[8] The Euler–Lagrange approach can be further subdivided to the Discrete Particle method (DPM), Multiphase-Particle-in-Cell method (MP-PIC), Dense Discrete Phase Model incorporated with Kinetic Theory of Granular Flow (DDPM-KTGF), and CFD-Discrete Element Method (CFD-DEM), which differ in their treatment of the particle–particle interaction.[9]

Due to the advantages of the Euler–Lagrange approach with regard to computational efficiency and accuracy, it has been widely used for the simulation of gas–solid flows. For instance, Wang et al.[10] applied the Euler–Lagrange method along with the MP-PIC approach for a cold circulating fluidized bed (CFB) with a loop seal and studied the effects of grid resolution, drag model, and particle size distribution (PSD) on the hydrodynamic behavior of a circulating fluidized bed (CFB). The model setups were then used to study the influence of operating parameters, including loop seal aeration rate, fluidized air velocity in the riser and total bed inventory, on the solid circulation characteristics.[11] In Ref. 12, a CFB combustor under cold flow condition has been calculated using the CPFD method coupled with different drag models, and the results showed good agreement with experiments for varied bed inventory. Zafiryadis et al.[13] applied the Euler–Lagrange method along with the MP-PIC approach for a cold flow CFB, where the pressure constant and the exponent of the MP-PIC particle stress model were found to have the largest influence on correctly reproducing the fluidization behavior. A biomass gasification plant in cold flow operation has been simulated by Lunzer et al.[14] with the Euler–Lagrange/MP-PIC method and different drag models, which revealed a significant impact of the particle size distribution. Furthermore, the model constant for the particle stress used by the MP-PIC approach was found to play an important role in close-packed regions. Wu et al.[15] employed the dense discrete phase model (DDPM) to investigate flow dynamics in a swirling gas–solid fluidized bed, which results in a decreased bed height and pressure drop compared with general setups without using a swirling gas flow. Moreover, different operation regimes have been identified with increasing superficial velocity and an increase in the operation velocity was found to be more beneficial in terms of particle mixing in the swirling fluidized bed. In Ref. 16, two models for considering heat transfer close to the walls of fluidized beds have been introduced in the framework of the CFD-DEM (discrete element method) approach and were validated with experimental results. A review on the simulation of cold flow fluidized beds has been provided in Ref. 17, and the influence of some key models such as inter-phase drag model has been highlighted.

Another class of modeling gas–solid flows is given by the particle-resolved direct numerical simulation (PR-DNS),[18] which represents the most accurate, but also the most computationally expensive method due to the resolution of the flow field around the particle, including its boundary layer. By using PR-DNS, Moriche et al.[19] have

studied the clustering of oblate spheroids settling in ambient fluid. Tenneti et al.[20] has applied PR-DNS to study the acceleration of particles due to gas–solid and inter-particle interactions by means of the particle velocity variance (granular temperature). Esteghamatian et al.[21] have performed particle-resolved simulations for liquid/solid and gas/solid fluidization, which revealed non-isotropic mechanisms for driving the particle motion and the dominance of diffusive and convective mechanisms.

In addition, a large number of works have focused on improving the accuracy of the Euler–Lagrange method along with its submodels. In particular, great efforts have been made to develop more sophisticated drag model as well as the quantification of uncertainties induced by the drag model.[22,24–28] Moreover, a computationally efficient particle cloud tracer method is presented in Ref. 23 for tracing a large number of particles and modeling statistic moments of particle groups in Euler–Lagrange formulations. Patel et al.[29] have compared the performance of TFM and Euler–Lagrange methods, where the convergence of the methods under grid refinement is found to depend on the simulation method and the specific case of concern. The problem of large particle-size to mesh-spacing ratio in dilute particle-laden flows has been studied by Evrard et al.[30] Similar work has been conducted in Ref. 31, where a strategy for simulating particle-laden flows using cell sizes smaller than the particle diameter has been proposed. A comprehensive review on the development of mathematical models for gas–solid flows as well as their applications to fluidized beds has been presented in Ref. 9, which confirms the capability of numerical models for designing industrial plants based on the fluidized bed technology.

As the gas–solid and solid–solid interactions occur over a wide range of length and time scales and are affected by a large number of operational, dimensional, and design parameters, the functional dependence of fluidized bed characteristics on these design parameters still have large uncertainties. Therefore, despite the achieved progress in recent works, detailed knowledge with regard to accurate prediction of the hydrodynamic behavior of fluidized beds is missing. In particular, most of the previous numerical works have focused on the validation of specific sub-models or model parameters and studying the influence of operational parameters on the overall behavior of the considered fluidized bed. However, in general, it is not sufficient to solely use general features such as bed height, pressure drop, or solid circulation rate for characterizing the temporally developing, multi-scale gas–solid system within the fluidized bed, as these are not directly related to the performance of fluidized beds in terms of an efficient mixing or heating. In order to gain more detailed knowledge of the hydrodynamic process of the fluidized bed, highly resolved numerical simulations have been conducted for a laboratory-scale fluidized bed at isothermal condition. Objective of this work is to evaluate its unsteady dynamic properties in terms of the specific kinetic energy of the bed material and the bubble frequency. The specific kinetic energy is equivalent with the averaged moving velocity of the bed material within the fluidized bed, which can be regarded as a measure for the efficiency of the multiphase momentum exchange from the gas to the solid phase. On the other hand, the bubble frequency represents a measure for the characteristic dominating timescale of the bubbles within fluidized bed system. The correlations of these properties with the operating parameters have been quantitatively evaluated, which reveals their usefulness for a more detailed assessment of the hydrodynamics of fluidized beds.

II. SIMULATION METHODS

A. Euler–Lagrange approach for simulation of gas-solid flows

As a detailed resolution of each solid particle including its boundary layer in a fluidized bed is computationally too expensive, a hybrid Euler–Lagrange approach is used in the present work for modeling the multiphase interactions.[32] In this method, the gas flow is regarded as a continuous phase, which is modeled by means of the Naiver–Stokes equations. The solid particles are treated as dispersed, and their trajectories are calculated based on a balance of forces acting on the particle, along with the equation of motion. Both sets of Euler and Lagrange equations concerning the gas and solid phase are coupled via source terms for considering the transfer of momentum between the different phases.

For the continuous gas phase, the following balance equations for total mass and momentum are solved[9]

$$\frac{\partial \varepsilon \rho_g}{\partial t} + \nabla \cdot (\varepsilon \rho_g \vec{u}_g) = 0, \tag{1}$$

$$\frac{\partial \varepsilon \rho_g \vec{u}_g}{\partial t} + \nabla \cdot (\varepsilon \rho_g \vec{u}_g \vec{u}_g) = -\nabla p + \nabla \cdot (\varepsilon \overline{\tau}_{eff}) + \varepsilon \rho_g \vec{g} + \vec{S}_{p,mom} \tag{2}$$

with the volume fraction of gas ε (also call void fraction or porosity) and the gas density ρ_g; $\vec{u}_g$ is the gas velocity and $\vec{g}$ is the gravitational acceleration. p is the pressure. The effective stress tensor is calculated from

$$\overline{\tau}_{eff} = \mu_g (\nabla \vec{u}_g + \nabla \vec{u}_g^T) - \frac{2}{3} \mu_g (\nabla \cdot \vec{u}_g) \overline{I} \tag{3}$$

with μ_g and $\overline{I}$ being the dynamic viscosity of the gas phase and the identity matrix. The momentum exchange between the continuous and disperse phases in Eq. (2) is given by the source term $\vec{S}_{p,mom}$

$$\vec{S}_{p,mom} = \sum_{i=1}^{n_{p,cell}} \frac{\vec{F}_{d,i}}{V_{cell}}, \tag{4}$$

which represents the sum of the drag forces acting on all particles $\vec{F}_{d,i}$ within the cell volume V_{cell}, with $n_{p,cell}$ being the number of the particles in the current computational cell. No turbulence model has been used for the simulation, i.e., the gas flow has been regarded as laminar, as the Reynolds number Re based on the reactor diameter and the bulk flow velocity is lower than 2000 for all considered cases in this work (see Sec. III A).

The momentum equation for each discrete particle follows Newton's second axiom,[9] where the acceleration of the ith particle is due to external forces exerted on the particle

$$m_{p,i} \frac{\partial \vec{u}_{p,i}}{\partial t} = \vec{F}_{d,i} + \vec{F}_{g,i} + \vec{F}_{c,i} + \vec{F}_{i,i}. \tag{5}$$

The particle positions are then obtained from time integration of the particle velocity $\vec{u}_{p,i}$ with the help of the equation of motion

$$\frac{d\vec{x}_{p,i}}{dt} = \vec{u}_{p,i}. \tag{6}$$

In Eqs. (5) and (6), $m_{p,i}$ and $\vec{x}_{p,i}$ represent the mass and position vector of the ith particle; $\vec{F}_{c,i}$ corresponds to the force due to inter-particle collisions, and $\vec{F}_{g,i}$ is the buoyancy force

$$\vec{F}_{g,i} = m_{p,i} \cdot \vec{g} \cdot \left(1 - \frac{\rho_g}{\rho_{p,i}}\right) \tag{7}$$

with the particle density $\rho_{p,i}$. $\vec{F}_{i,i}$ in Eq. (5) is representative for other inertial forces that can act on a particle, such as centrifugal or electromagnetic force. The drag force $\vec{F}_{d,i}$ is calculated from the Ergun–Wen–Yu model[5,9]

$$\vec{F}_{d,i} = \begin{cases} \frac{3}{4} C_d \frac{\rho_g(1-\varepsilon)\varepsilon^{-1.65}}{d_{p,i}} |\vec{u}_g - \vec{u}_{p,i}|, & \varepsilon \geq 0.8, \\ 150 \frac{\mu_g(1-\varepsilon)^2}{\varepsilon d_p^2} + 1.75 \frac{\rho_g(1-\varepsilon)|\vec{u}_g - \vec{u}_{p,i}|}{\varepsilon d_{p,i}}, & \varepsilon < 0.8, \end{cases} \tag{8}$$

with the particle diameter $d_{p,i}$ and the gas-phase dynamic viscosity μ_g. The drag coefficient C_d is calculated as a function of the particle Reynolds number Re_p and void fraction[9]

$$C_d = \begin{cases} \frac{24}{\varepsilon Re_p}(1 + 0.15(\varepsilon \cdot Re_p)^{0.687}) & Re_p \leq 1000, \\ 0.44 & Re > 1000. \end{cases} \tag{9}$$

B. Modeling of inter-particle collisions

As the Discrete Element Method (DEM) or the Discrete Particle Method (DPM) for modeling the inter-particular force is computationally too expensive due to the evaluation of the collision force based on contact detection of all individual particles,[33] the Multi-phase Particle in Cell (MP-PIC) concept has been used to model the particle collisions. In addition, the MP-PIC method uses the parcel concept, where each parcel represents a collective of a number of particles with the same size and velocity. In this way, the collision force between the particles is given by

$$\vec{F}_{c,i} = \frac{m_{p,i}}{\alpha_p \rho_{p,i}} \nabla \tau_p \tag{10}$$

with the particle stress τ_p calculated according to the modified Harris–Crighton model[34,35]

$$\tau_p = \frac{p_s \cdot \alpha_p^\beta}{\mathbf{max}(\varepsilon, \alpha_{packed} - \alpha_p)}, \tag{11}$$

where α_p is the volume fraction of solid phase. p_s is a model constant called the normal particle stress; β represents an empirical exponent and α_{packed} corresponds to the particle-close-pack volume fraction at the densest packing, which represents the largest possible volume fraction of the solid phase. Through parameter studies using $1 \leq p_S \leq 50$ and $2 \leq \beta \leq 5$ according to Ref. 35, $p_s = 10$ Pa and $\beta = 2$ have been found to show the best agreement with the measured pressure drop, which are, therefore, used in the current work. The close-pack limit α_{packed} depends on the size, shape, and ordering of the particles, which is set to $\alpha_{packed} = 0.65$ assuming randomly packed spheres.[36] A small value for ε is used to avoid division by zero, i.e., $\varepsilon = 10^{-7}$. Off-center particle collisions result in scattering of the particles in all spatial directions. This effect has been considered by an isotropy model, which corrects the velocity of the particle based on a stochastic process.[37]

07 March 2024 15:33:09

Particle–wall collisions are modeled with a rebound model, where the velocity of each particle after collision with a wall is calculated from

$$\begin{pmatrix} u_{new,t} \\ u_{new,n} \end{pmatrix} = \begin{pmatrix} u_{old,t} \\ u_{old,n} \end{pmatrix} - (1+e) \begin{pmatrix} 0 \\ u_{old,n} \end{pmatrix} - \mu \begin{pmatrix} u_{old,t} \\ 0 \end{pmatrix}, \quad (12)$$

where $(u_{new,t}, u_{new,n})^t$ are the newly calculated particle velocities in the tangential and normal direction with respect to the wall. $(u_{old,t}, u_{old,n})^t$ are the particle velocities before the collision; e is the coefficient of elasticity for the normal direction to the wall and indicates elasticity of the impact. For $e = 1$, the impact is fully elastic, and for $e = 0$, the impact is plastic. The same applies to the restitution coefficient μ, where $\mu = 0$ indicates a fully elastic and $\mu = 1$ a fully plastic impact.

III. SIMULATION SETUPS

A. Operating conditions

The laboratory-scale fluidized bed reactor considered in this work has a cylindrical geometry with a diameter of 5 cm and a length of 100 cm. A porous sintered metal plate is used at the bottom of the reactor as gas distributor, which is permeable to the gas and generates homogeneous regular incoming gas flow toward the bed materials. Quasi-spherical silica sand particles with a Gaussian size distribution and an arithmetic mean diameter of 212 μm have been used as carrier material, along with nitrogen as fluidizing agent. Figure 1 on the left shows the experimental test rig along with a snapshot of the fluidized bed in cold-mode operation. The bulk gas flow velocity u_G has been varied from 13.6 to 29.7 cm/s and the bed inventory m_s from 195 to 586 g, as shown on the right of Fig. 1.

The operating parameters have been designed according to the Grace-diagram[38,40] to generate a bubbling fluidized bed considering an efficient mixing. In this way, the dimensionless superficial velocity $u_G^* = u_G \sqrt[3]{\frac{\rho_g^2}{\mu_g(\rho_s - \rho_g)g}}$ is within the range of $0.1 < u^* < 0.5$ (for $0.136 < u_G < 0.297$ m/s) along with a dimensionless particle
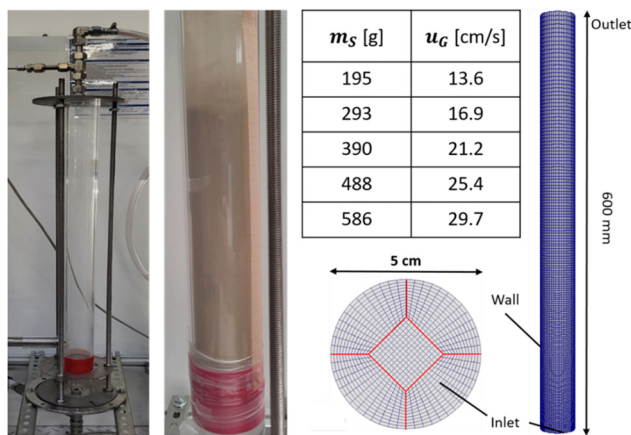

FIG. 1. Test rig used for the experimental study of a laboratory-scale fluidized bed (left) and topology of the computational grid used for the numerical simulations of the considered fluidized bed (right). The operating parameters with varied total sand mass m_S and superficial gas velocity u_G are given in the table.
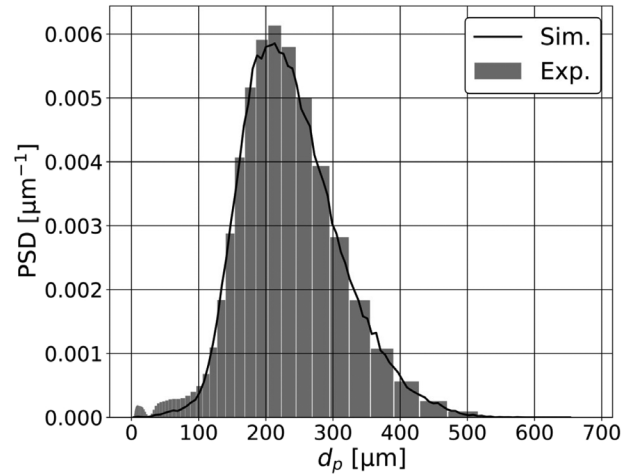

FIG. 2. Comparison of particle size distributions (PSD) in the experiments and simulations.

diameter at $d_P^* = d_P \sqrt[3]{\frac{\rho_g(\rho_s - \rho_g)g}{\mu_g^2}} = 10.24$ by using a mean particle diameter of $d_P = 0.21$ mm (see Fig. 2). By doing so, the operating conditions in terms of the dimensionless parameters can be applied to up-scaled fluidized beds for engineering applications, too.

B. Computational domain and resolutions

The computational domain used for the simulation is given by a cylinder, which has a length of 60 cm and a diameter of 5 cm. The dimensions of the domain have been selected to be sufficiently large to cover the whole fluidized bed at all considered operating conditions (the maximum bed height is approximately 30 cm, see Fig. 7). It is shorter than the tube used in the experiment (with 100 cm) in order to save computational cost. As shown in Fig. 1 on the right, the topology of the computational grid for the cross-sectional area is built with an O-type grid, which creates uniformly distributed grid cells from the center to the sidewall with an almost equidistant grid length of ca. 1 mm in the radial direction. The grid resolution in the axial direction is 1 mm at the ground of the tube, which increases with a small expansion factor in the streamwise direction. Overall, the length of the cylindrical domain has been resolved by 180 cells and the diameter of the tube with approximately 40 cells.

For the Euler–Lagrange simulation, a number of Lagrange particles (LPs) is injected from given locations, which are then tracked during the simulation. These LPs represent collections of spherical particles with the same characteristics, e.g., diameters and velocities. In this work, the LPs are initialized uniformly in space along the whole domain, which fall down due to gravity and interact with the incoming gas flow. A quasi steady-state solution with a fluidized sand bed is generated after about 1 s. The sizes of the particles are set according to the measured particle size distribution (PSD), which is shown in Fig. 2. The number of tracked LPs increases proportionally with the bed inventory, i.e., with $n_P \approx 2 \times 10^6$, 3×10^6, 4×10^6, 5×10^6, 6×10^6 for $m_G = 195, 293, 390, 488, 586$ g, leading to a constant number of particle per parcel for all cases. The grid resolution and the
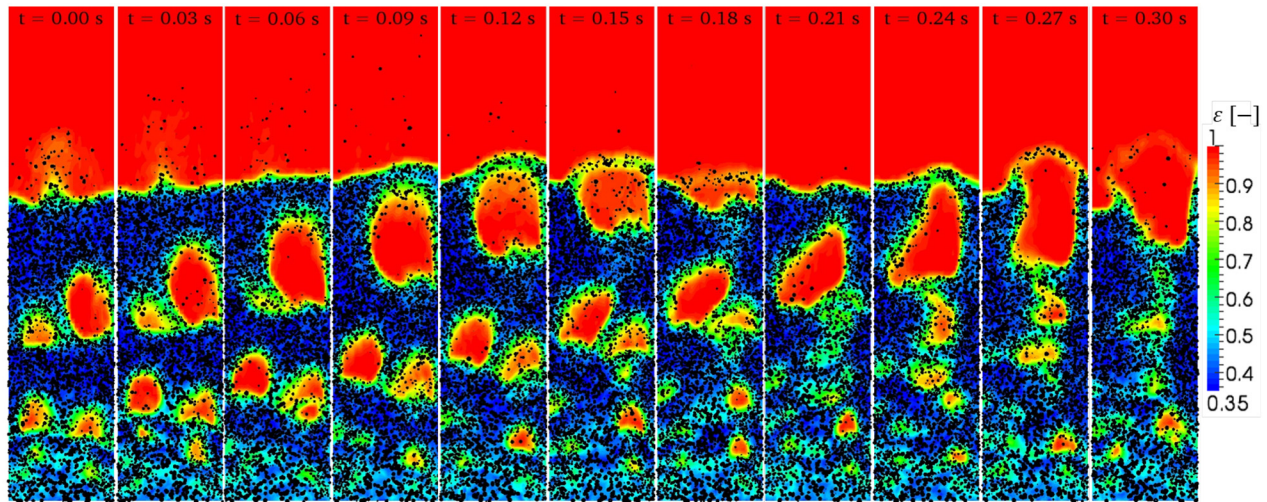
07 March 2024 15:33:09

FIG. 3. Snapshots of the void fraction for the case with $m_S = 390$ g and $u_G = 21$ cm/s on a cutting plane passing through the centerline axis.

number of LPs have been selected based on previous grid-independence studies and a compromise between simulation accuracy and computational cost, where a further refinement of the grid or increase in the number of LPs does not lead to a clear improvement with regard to comparison with the measured pressure drop.

C. Boundary conditions

The boundaries of the computational domain are indicated in Fig. 1 on the right, where nitrogen gas enters the domain from the inlet and leaves at the outlet. A non-slip condition is used for the reactor wall. The flow velocity at the inlet is calculated from $u_{inlet} = u_G/\varepsilon$ with ε being the void or gas volume fraction. In the case of $\varepsilon = 1$ or without sand particles, the inlet flow velocity is equal to u_G; if sand particles are available or $\varepsilon < 1$, the local flow velocity at the inlet is larger than u_G to preserve continuity. The pressure at the outlet is fixed at ambient pressure, whereas its gradient at the reactor wall and at the inlet is set to zero. The simulations have been conducted under isothermal condition at 20 °C and 1 atm. The densities of the gas and the sand are set to $\rho_G = 1.14$ and $\rho_S = 2660$ kg/m³.

The open-source code OpenFOAM-v2206[41] has been used to perform the numerical simulations, and the standard solver MP-PICFoam has been applied to simulate the gas–solid flow in the fluidized bed. The main reason for using MP-PICFoam in OpenFOAM is attributed to the fact that, compared with other commercial or open-source CFD codes, the solver can be extended more easily to model heat transfer and heterogeneous reactions in fluidized bed, which represent future work of the present study for simulation of plastic pyrolysis in fluidized beds. The balance equations are solved in an incompressible formulation, employing a second-order interpolation scheme for discretization of the convection and diffusion terms, along with an implicit scheme (Euler) for time integration. The time step was set to 0.1 ms, ensuring a maximum CFL (Courant–Friedrichs–Lewy) number smaller than unity. The simulations have been run for a physical time of 4 s, where statistical averaging of the flow has been performed for a physical time of 3 s after initialization of the fluidized bed.

IV. SIMULATION RESULTS

A. Morphology of the fluidized bed

Figure 3 depicts time series of the contours of the calculated void or gas fraction ε on a cutting plane passing through the centerline axis for the reference case with $m_S = 390$ g and $u_G = 21$ cm/s. The sand particles are indicated by the black dots, which are shown for a disk across the symmetry axis with a thickness of 1 mm. The time interval between the snapshots is 30 ms. Only a subset of the total particles is shown and the particles are scaled up by a factor of 5 for better visualization. The bubbles are illustrated by the red zones with large ε. The bubbling fluidization behavior observed in the experiment has been reproduced by the simulation. While the gas flow passes through the sand bed, small bubbles are first generated close to the bottom of the reactor and rise in streamwise direction due to buoyancy forces. With increased axial distance, the size of bubbles increases due to coalescence of the small bubbles until they reach the upper surface of the fluidized bed.

As the bubbles rise along the centerline axis, the sand particles are driven to the wall side. Because the gas flow velocity is low close to the wall due to the non-slip condition, the particles fall down along the wall. Near to the base of the reactor, the sand particles interact with the incoming gas flow and are pushed upwardly by the initial small bubbles. As shown in Fig. 4 by the contours of time-averaged solid fraction $\bar{\alpha}_P$ and streamwise flow velocity $\bar{u}$, the circulation of the sand particles leads to a core–annulus flow pattern, where the gas bubbles dominate the core region and the particles are concentrated close to the wall. In addition, a negative correlation between the $\bar{\alpha}_P$ and $\bar{u}$ can be identified. In the core region, the share of particles is lowest and the gas flow velocity is largest, whereas the reversed trend is found in the near-wall region. At the upper surface of the fluidized bed, a small portion of sand particles is ejected from the fluidized bed due to bursting of the bubbles.

Figure 5 shows instantaneous contours of ε on a meridian cutting plane passing through the centerline axis for varied u_G from 14 to 30 cm/s panel 5(a) and for varied m_S from 195 to 586 g panel 5(b). The case with the smallest u_G at 14 cm/s shows a smooth or close-to-minimum fluidization behavior, where the sand bed is only
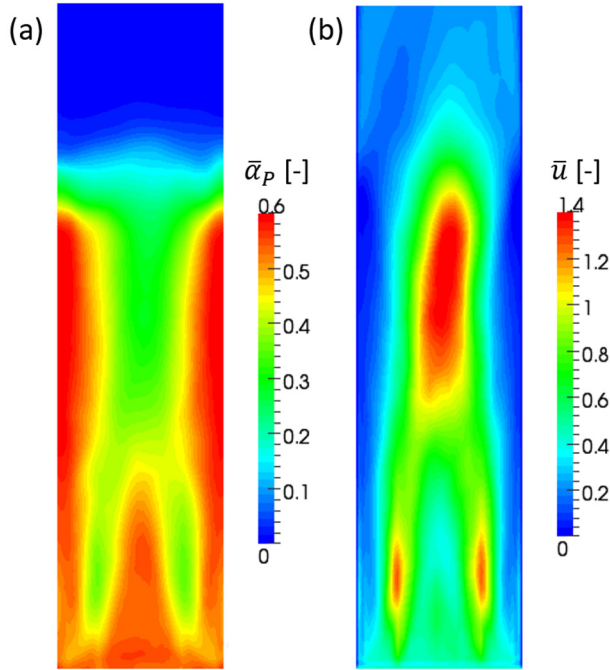
FIG. 4. Contours of time-averaged particle volume fraction and gas flow velocity for the case with $m_S = 390$ g and $u_G = 21$ cm/s.
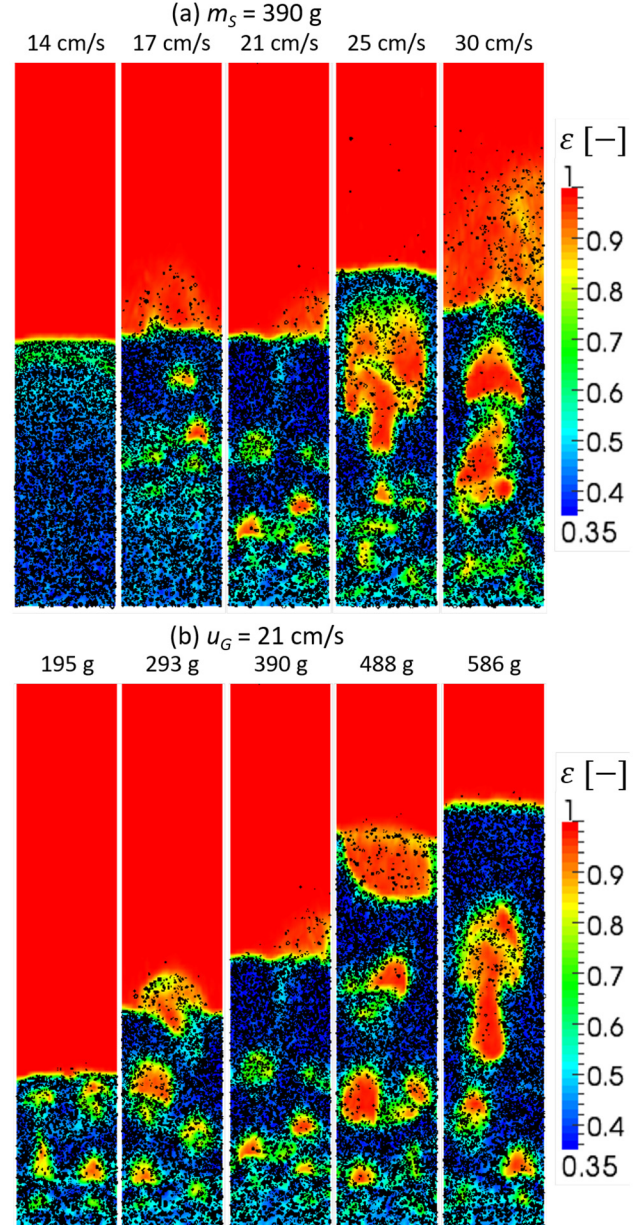

FIG. 5. Snapshots of void fraction on a cutting plane passing through the centerline axis at increasing superficial gas flow velocity (a) and at increasing bed inventory (b).

weakly fluidized without forming clear bubbles. A further increase in u_G results in the formation of bubbles, corresponding to the bubbling fluidization regime. These bubbles rise along the axial direction due to buoyancy and collapse at the upper boundary of the fluidized bed. The size of the generated bubbles increases with u_G and becomes as large as the reactor diameter at large u_G. The enhanced bubble formation at larger u_G is attributed to the increased momentum of the gas flow, leading to a reinforced gas-to-solid momentum transfer and recirculation of the sand particles. The onset of a slugging type fluidization can be observed at $u_G = 30$ cm/s, with a large number of particles thrown away by the fluidized bed.

As shown in Fig. 5(b), the volume of the fluidized bed expands while increasing m_S at constant $u_G = 21$ cm/s, which indicates an increase in the bed height h_B. As the volume of the fluidized bed increases with m_S, the small bubbles generated near the ground of the reactor have more space to develop and to coalesce with each other so that the size of the bubbles increases with m_S.

The operating parameters used in the experiment are designed to establish the bubbling fluidization regime, which is confirmed in the numerical simulations. However, a direct comparison of the bubble formation and the particle circulation between experiment and simulation is not possible due to limitations given by the line-of-sight measurement techniques. The desired bubbling fluidization regime can be achieved for a moderate range of u_G and m_S, which is beneficial with regard to an efficient mixing and heat-/mass transfer.

B. Pressure drop and bed height

While passing through the sand bed, the gas flow yields a pressure drop Δp due to the loss of momentum and kinetic energy, which

are transferred to the solid phase. In the fixed bed regime, Δp increases linearly with u_G.[42] For u_G larger than the minimum fluidization velocity, the solid particles are carried by the gas flow and attain a fluid-like behavior. In this case, the pressure loss of the fluid when flowing through the bed is equal to the weight of the bed per unit area of the bed cross-section[42,43]

$$\Delta p = \frac{F_g - F_A}{A_0} = \frac{V_S \cdot (\rho_S - \rho_G) \cdot g}{A_0} = h_B \cdot (1 - \varepsilon) \cdot (\rho_S - \rho_G) \cdot g, \quad (13)$$

07 March 2024 15:33:09

where F_g and F_A are the gravitational and buoyancy force, A_0 and V_S are the cross-sectional area and the total volume of sand particles. Figure 6(a) compares the measured and calculated Δp, which show a reasonably good agreement. As the bed height h_B is not sensitive to u_G, as shown in Fig. 5(a), Δp increases slightly or remains almost constant with u_G. In contrast, Δp increases with the bed inventory or m_S due to the increased bed height or mass of sand, respectively.

Figure 6(b) depicts the normalized pressure drop Δp^* with regard to the total mass of sand

$$\Delta p^* = \frac{\Delta p}{\rho_S g L}, \quad L = \frac{m_S}{A_0 \rho_S}, \quad (14)$$

where Δp^* calculated from different m_S is almost constant, indicating a quasi-proportional correlation of Δp with m_S. However, Δp from the simulations is underestimated compared with the measurements. This could be attributed to the assumptions used in the simulations which predict a lower energy loss for the gas–solid system. For instance, the

particles are assumed to have ideal spherical shape and the angular momentum of the particles has not been considered. Moreover, the frictional energy loss during the particle–particle and particle–wall collisions has not been modeled in a detailed way due to the use of the rebound model. Therefore, the energy loss caused by the whole solid–gas system is underestimated. In addition, the results may be improved by a more sophisticated drag model. The difference between calculated and measured Δp is less than 20% for all cases, which increases with m_S, because the effect of energy loss becomes more pronounced for large m_S. Despite the discrepancies between experiments and simulations for Δp, the hydrodynamic behavior with regard to the fluidization behavior of the considered fluidized bed has been reproduced adequately, which validates the numerical approach used in this work.

Figures 7(a) and 7(b) depicts profiles of time-averaged particle volume fraction $\bar{\alpha}_P$ along the centerline axis for constant m_S at 390 g with varied u_G and for constant u_G at 21 cm/s with varied m_S. For the case with $u_G = 13.6$ cm/s, the fluidized bed is in the close-to-minimum fluidization regime, without clear formation of bubbles, as shown in Fig. 5(a) on the left. Therefore, $\bar{\alpha}_P$ yields an almost constant
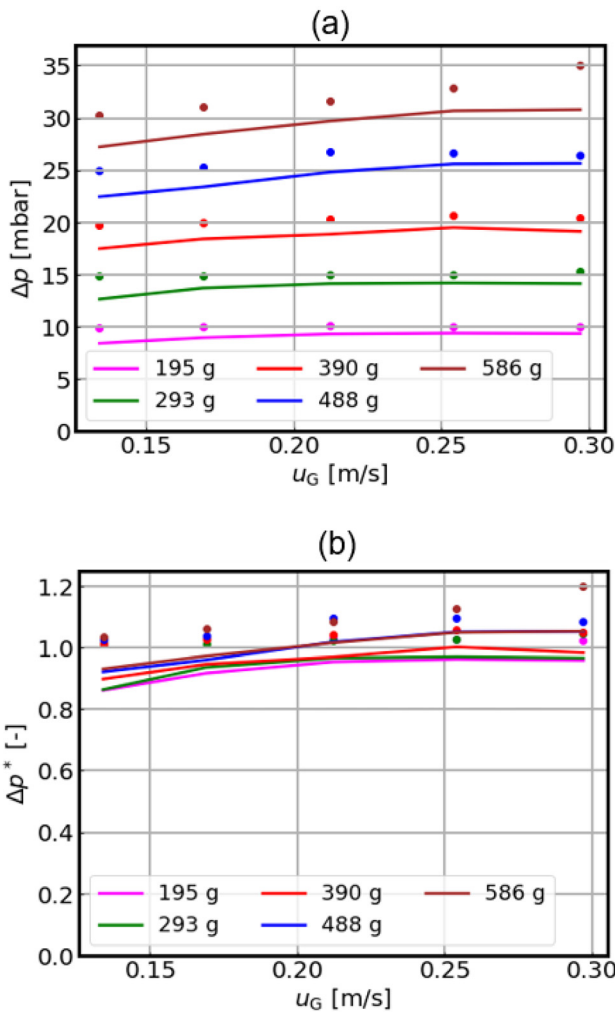

FIG. 6. Comparison of measured (points) and calculated pressure drop at different operating conditions.
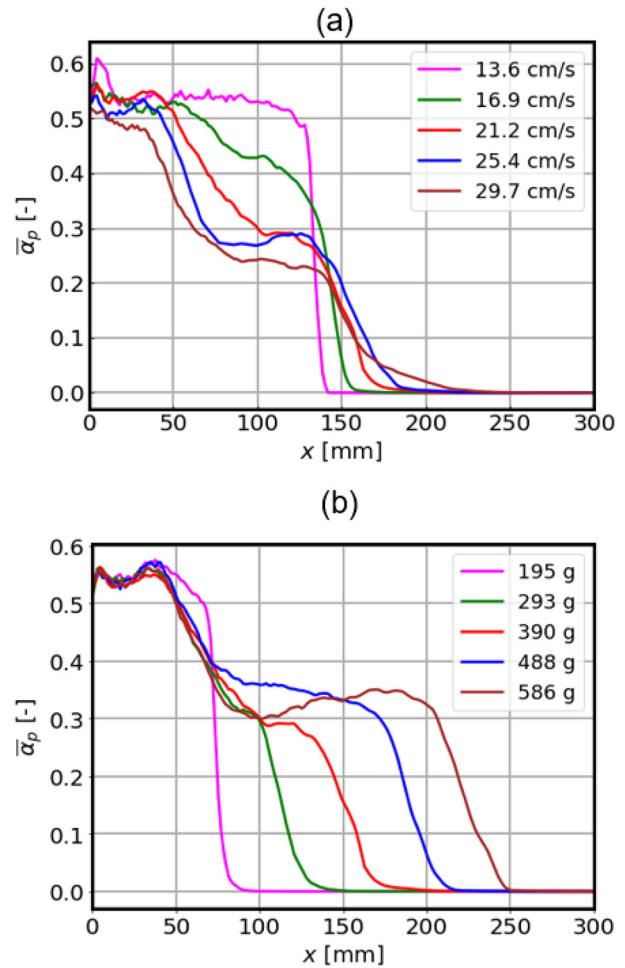

FIG. 7. Axial profiles of time-averaged particle volume fraction along the centerline axis at different superficial gas velocity (a) and sand mass (b).

07 March 2024 15:33:09

distribution over the whole bed height at $\bar{\alpha}_p \approx 0.53$ for $u_G = 13.6$ cm/s, which decreases rapidly to 0 while approaching the upper surface of the bed. With further increased u_G, the fluidized bed is characterized by the bubbling fluidization regime. In this case, $\bar{\alpha}_p$ is largest at the base of the reactor and decreases gradually to 0 at the upper surface of the sand bed. Figure 7(b) shows profiles of $\bar{\alpha}_p$ for varied m_S, which are similar in the lower part of the fluidized bed with $x < 70$ mm. Therefore, the behavior of initial bubble formation near to the bottom of the fluidized bed is similar for all cases due to the use of a constant u_G, as shown in Fig. 5(b). However, $\bar{\alpha}_p$ decreases more slowly further downstream at larger m_S, indicating an increase in the bed height h_B with m_S. Due to the large-scale bubbles generated at the centerline axis, $\bar{\alpha}_p$ increases in the radial direction and reaches its maximum in a region close to the wall.

C. Specific kinetic energy of bed material

The intense contact between gas and solid as well as the intermixing of particulate phase with frequent particle–particle collisions prevails the hydrodynamics of the fluidized bed. The momentum of the gas phase is transferred to the solid particles through aerodynamic forces or drag, respectively, which leads to a chaotic motion of the particles and an increase in the solid-phase kinetic energy. Therefore, the total kinetic energy available in the solid phase represents a suitable measure for the effectiveness of momentum transfer or mixing between both phases. In order to access this behavior more quantitatively, the specific kinetic energy of the bed inventory k_S in the fluidized bed has been evaluated by summing up the kinetic energies of all solid particles

$$k_S = \frac{1}{m_S} \sum_{i=1}^{N_p} m_{p,i} u_{p,i}^2 / 2 \tag{15}$$

with the mass and velocity of each sand particle $m_{p,i}$ and $u_{p,i}$. In this way, k_S represents an integral parameter, which measures the kinetic energy of all sand particles available in the fluidized bed.

Figure 8(a) depicts the temporal evolution of the calculated k_S at $m_S = 390$ g and with varied u_G, which fluctuates over time. Figure 8(b) shows the time-averaged k_S at varied m_S and u_G. k_S increases with u_G, which is attributed to the increased momentum flux of the gas flow, leading to a reinforced momentum transfer from the gas to the solid phase. Moreover, $\bar{k}_S$ increases with m_S, as shown in Fig. 8(b), which indicates a stronger momentum exchange between the gas and solid phases in the case of increased bed inventory. This could be attributable to the increased contact surface area between the gas and solid phases.

D. Bubble frequency

The periodically rising bubbles and the collapse of these bubbles at the upper side of the fluidized bed trigger the whole system into a pulsating mode. The dominating bubble frequency f_B corresponds to the number of repetitions of the recurring bubbles within one second and represents a measure for the averaged moving speed or dynamics of the gas bubbles. The higher the bubble frequency, the more intense is the mixing process. Figure 9(a) shows the calculated temporal evolution of k_S for a constant gas velocity $u_G = 21$ cm/s and different sand mass m_S, which exhibit distinct periodical fluctuations. The number of repetitions of k_S decreases with m_S, which indicates a decrease in f_B
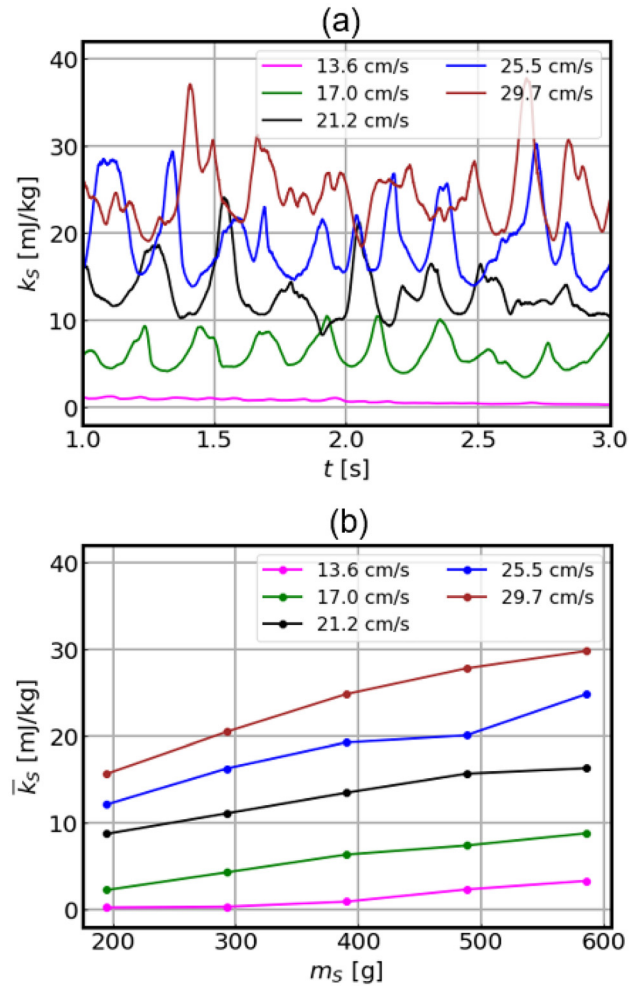

FIG. 8. Time evolution of specific kinetic energy of solid particles (a) and correlations of the time-mean specific kinetic energy with m_S at different u_G (b).

with m_S. This is due to the fact that the fluidized sand bed expands with increased bed inventory, as shown by the instantaneous contour of ε in Fig. 5(b). In the cases with small m_S, the height of fluidized bed is low and dominated by a number of small bubbles, which travel along a shorter distance up to the upper surface of the fluidized bed. This results in a shorter residence time of the bubbles or a higher bubble frequency, respectively. As the bed height increases with m_S, the small bubbles coalesce with each other while rising to the top of the fluidized bed. Therefore, the distance or time required for the bubbles to move through the bed volume is increased with m_S, leading to a decreased f_B. The bubble frequency f_B has been evaluated from spectral analysis (Fourier transformation) of the temporal development of k_S and plotted against m_S in Fig. 9(b), which yields a decrease with m_S. Under the current conditions, the fluidized bed is dominated by f_B in a relatively low frequency range between 2 and 7 Hz, which is attributed to the low gas flow velocity.

In summary, the bed height h_B and pressure drop Δp increase with m_S, whereas u_G has a subordinate effect on h_B and Δp. However,
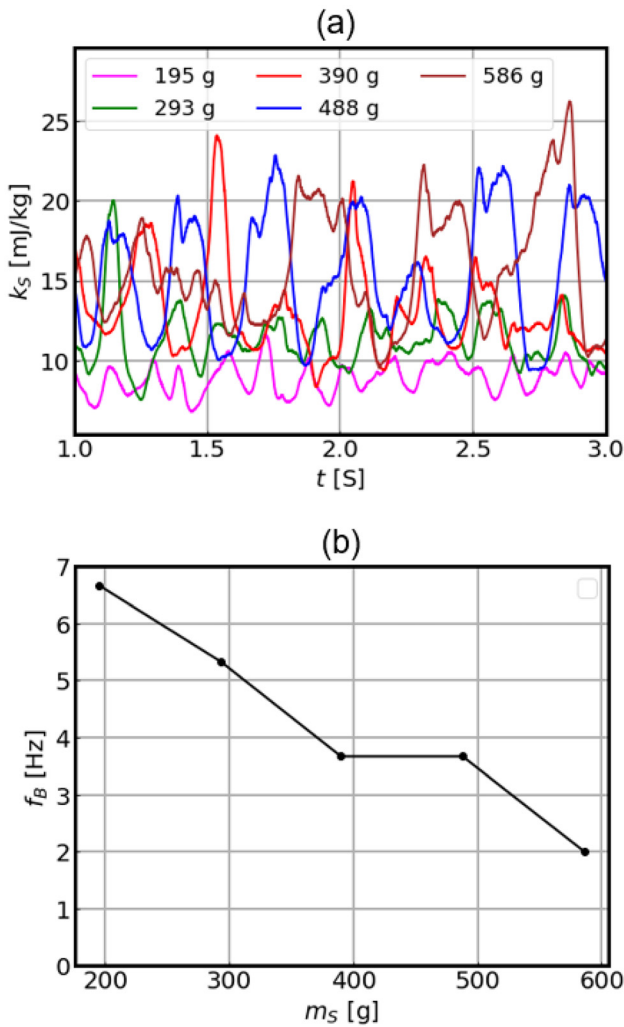
FIG. 9. Temporal evolution of specific kinetic energy at varying sand mass (a) and effect of bed inventory on bubble frequency (b).
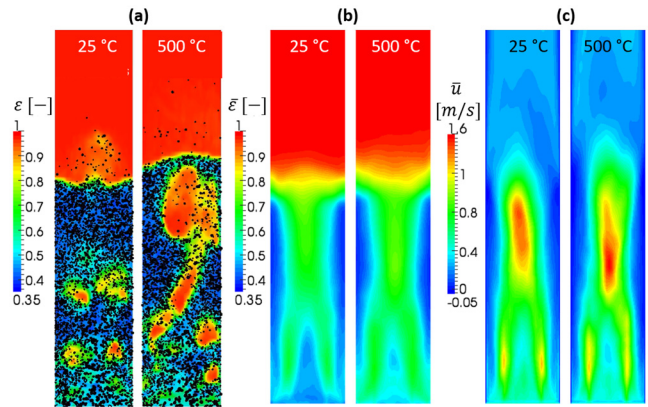

FIG. 10. Comparison of instantaneous contours of void fraction (a), time-mean contours of the void fraction (b), and time-mean contours of streamwise gas velocity (c) at $T_G = 20\,^\circ$C and $T_G = 500\,^\circ$C.

u_G has a strong impact on the fluidization behavior and, the specific kinetic energy of sand k_S increases with u_G, as shown in Fig. 8. In addition, the bubble frequency f_B decreases with m_S due to the increased bed volume, whereas f_B is not sensitive to u_G. The results reveal strong correlations of k_S and f_B with the general operating parameters m_S and u_G, which can be used for characterizing the hydrodynamics of fluidized beds in addition to h_B and Δp.

E. Effect of gas temperature

Fluidized beds are often operated at high-temperature condition like for drying, combustion, or gasification. The current fluidized bed has been designed for recycling of plastic wastes via pyrolysis process in the range of 400–600 °C.[44] Therefore, in order to study the behavior of k_S and f_B at elevated operating temperatures, an additional simulation has been conducted at a gas–solid temperature of $T_G = 500\,^\circ$C, while the bed inventory and superficial velocity have been kept

constant at $m_S = 390$ g and $u_G = 21$ cm/s. In this way, the density of the nitrogen gas decreases from $\rho_G = 1.14$ kg/m³ at 20 °C to $\rho_G = 0.44$ kg/m³ at $T_G = 500\,^\circ$C and the kinetic viscosity of the gas increases from 1.5×10^{-6} to 8.0×10^{-6} m²/s.

Figure 10(a) compares instantaneous contours of the void fraction ε on a meridian cutting plane passing through the symmetry axis. As m_S and u_G are kept constant, the bubbling fluidization regime remains almost unchanged at elevated temperature. Figures 10(b) and 10(c) show the time-averaged contours of ε and streamwise velocity of the gas phase on the same cutting plane, which reveal similar distributions at different T_G. Moreover, the bed height h_B is increased slightly with T_G, which leads to a slight increase in the pressure drop at elevated reactor temperature. This is attributed to the increased density difference or buoyancy force, respectively.

Figure 11(a) compares the temporal developments of the specific kinetic energy k_S at different T_G, where an increase in k_S with T_G can be detected. The time-averaged k_S is increased from $\bar{k}_S = 13.6$ mJ/kg at 20 °C to $\bar{k}_S = 19.2$ mJ/kg at 500 °C, which is more than 40%. The results reveal that the particles move with a higher velocity on average in the case of elevated temperature. The reason is given by the strongly increased kinetic viscosity of the gas phase, which causes a higher drag force exerted by the gas flow on the particles. As shown in Fig. 11(b), the volume-specific drag force calculated from Eq. (8) at given particle volume fractions $\alpha_P = 0.2$–0.4 and using a particle diameter of 0.2 mm increases with T_G, indicating a reinforced multiphase momentum exchange. The bubble frequency remains almost unchanged with T_G, which can be detected from the number of repetitions of k_S in the time evolution of k_S shown in Fig. 11(a).

F. Effect of up-scaling

The scale-up has often proven to be a significant obstacle in the development of new fluidized bed processes in the past, as reactors designed based on measurements from small laboratory apparatuses did not achieve the expected reaction rate at the operational scale. The cause of this well-known effect, which in its magnitude was never calculable in the past, is ultimately characterized by changes in fluid mechanics with increasing fluidized bed diameter. To study the effect
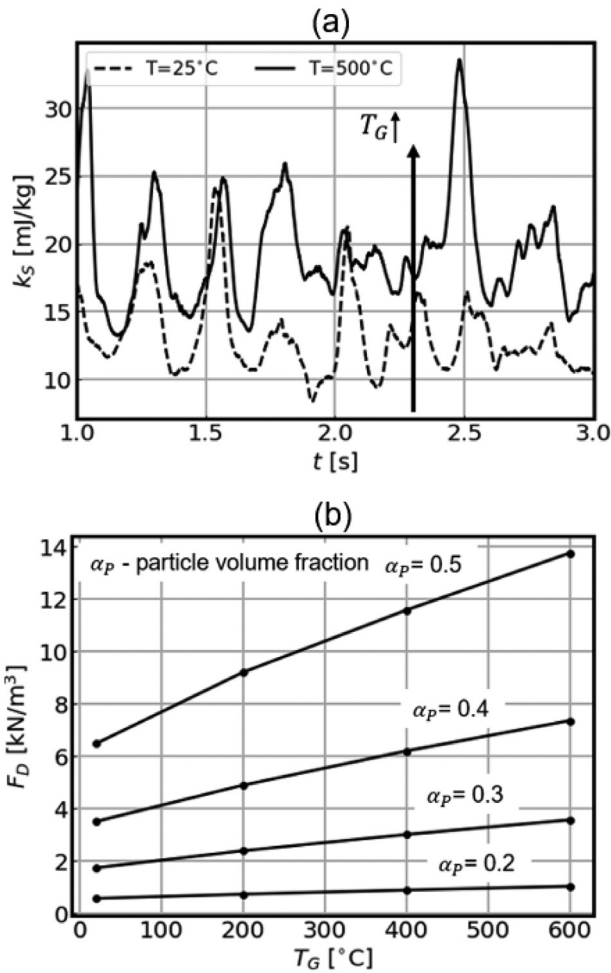
FIG. 11. Comparison of temporal evolution of specific kinetic energy at different gas temperature (a) and correlation of specific drag force with gas temperature (b).

FIG. 12. Grace diagram used for studying up-scaled fluidized bed.[39] Reproduced with permission from Schmid *et al.*, Biomass Convers. Biorefin. 2, 229–244 (2012). Copyright 2012 Springer Nature.

of up-scaling on the hydrodynamic properties of fluidized beds, the reactor diameter d_R has been scaled up to 3, 5, and 10 cm. The pressure drop and the bed height have been kept constant while up-scaling the fluidized bed, leading to an increased bed inventory. At the same time, the superficial velocity has been kept constant so that the same operating point within the bubbling fluidization regime from the Grace-diagram[38] can be achieved, as shown in Fig. 12 with the dimensionless superficial velocity of $u_G^* = 0.3$ and the dimensionless particle diameter of $d_P^* = 10.2$. In this way, the bed inventory increases with the reactor diameter by $m_S \propto d_R^2$, whereas the bubbling fluidization regime is retained. For the numerical simulation, the height of the domain as well as the grid resolution in the radial direction was kept constant at 60 cm and 1 mm while up-scaling the reactor. This leads to a proportional increase in the total number of grid cells n_C with m_S. In addition, the number of Lagrange parcels n_P increases linearly with m_S. The parameters used for the current study of up-scaling are listed in Table I.

Figures 13(a) and 13(b) depict snapshots of iso-contour of $\varepsilon = 0.66$ for different reactor sizes, which illustrate 3D structures of
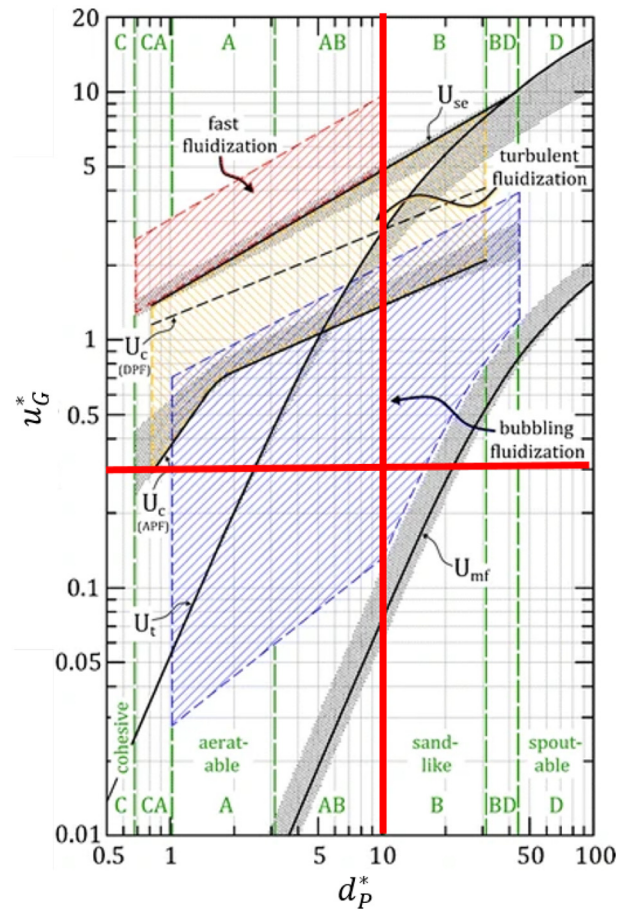
TABLE I. Bed inventory, superficial gas velocity, cell number, and parcel number used for simulation of up-scaled fluidized bed.

d_R (cm)	3	5	10
m_S (g)	140	390	1600
u_G (m/s)	21	21	21
n_C (−)	57.600	152 100	562.500
n_P (×10^6)	2.9	8.0	32.0

the bubbles. The solid particles are shown additionally in the second row. For the cases with $d_R = 3$ and 5 cm, the hydrodynamics of the fluidized bed is dominated by large-scale bubbles with sizes similar to the reactor diameter. In contrast, the bubbles rise along multiple off-centered columns in the case of $d_R = 10$ cm. The bubbles coalesce with each other so that with increasing height above the gas distributor base, the average bubble size rapidly increases. In narrow fluidized bed vessels with small d_R, the bubbles fill quickly the entire cross section.
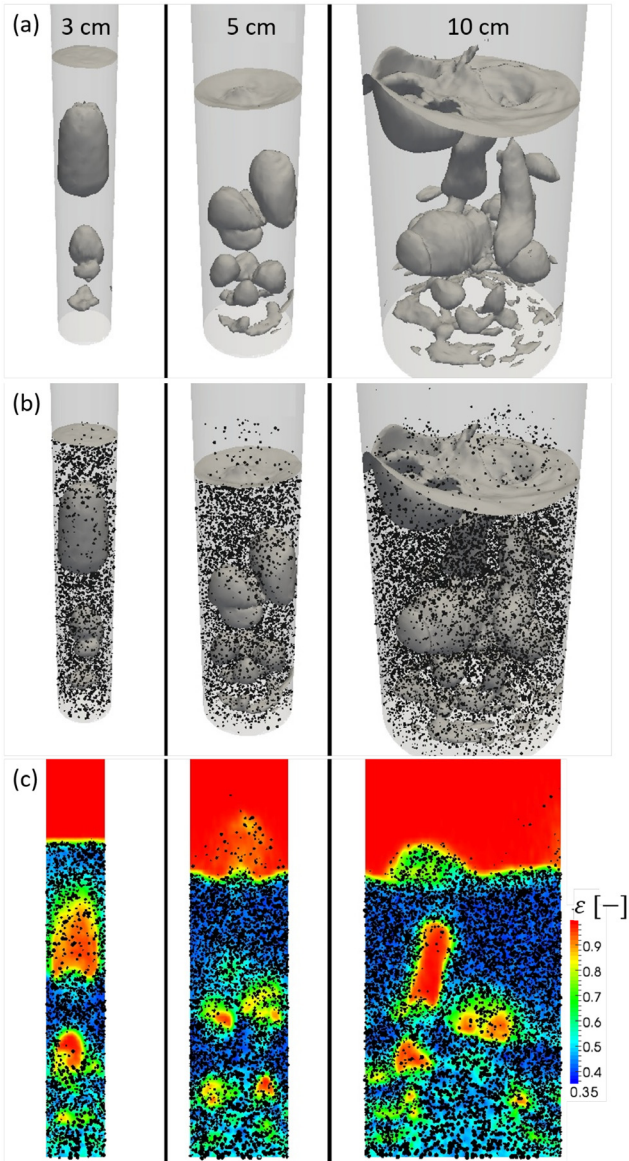
07 March 2024 15:33:09

FIG. 13. Iso-surfaces of $\varepsilon = 0.66$ for illustrating the bubble structure (a) and (b) and contours of ε on a cutting plane passing through the centerline axis (c) calculated with reactor diameters $d_R = 3$, 5, and 10 cm (from left to right).

The formation of bubbles is significantly stronger while using $d_R = 10$ cm, and the bubbles generally do not rise evenly distributed in the fluidized bed. Close to the base of fluidized bed, a near-wall zone with intensified bubble formation develops, which shifts toward the center of the pipe with increasing height above the distributor base. In the small fluidized bed, this shift leads quickly to large bubbles preferentially rising along the centerline axis of the reactor. The cause of this characteristic flow profile is the proximity of the reactor wall, which influences the coalescence process.

Figure 13(c) depicts calculated instantaneous contours of ε on a meridian cutting plane across the centerline axis for different reactor
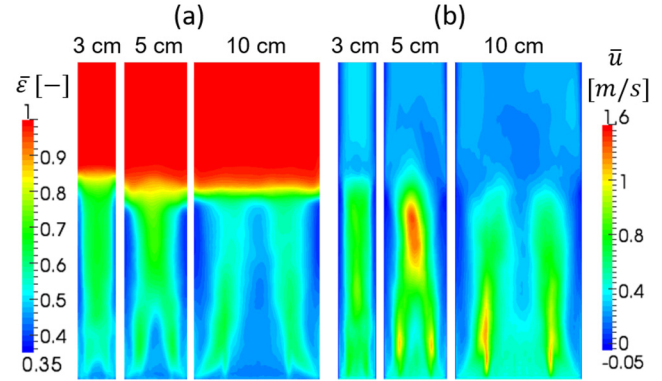

FIG. 14. Comparison of time-mean contours of the void fraction (a) and streamwise gas velocity (b) on a cutting plane passing through the centerline axis at varied reactor diameters.

sizes, where the sand particles are illustrated by the filled circles. For the smallest reactor with $d_R = 3$ cm, the fluidized bed is dominated by large bubbles rising along the centerline axis, whose size is similar to the diameter of the reactor. This is attributed to the narrow domain bounded by the reactor wall, which leads to a more intense coalescence of the initial small bubbles. At increased reactor size with $d_R = 5$ cm, there is more space between the large bubbles and the reactor wall, which allows formation of a low-speed region close to the wall and a recirculation of sand particles there. While further increasing the reactor size to $d_R = 10$ cm, the number of bubbles is increased significantly, and the bubbles rise along multiple columns without coalescing with each other further downstream. In this case, the gas flow recirculates additionally toward the symmetry axis, leading to an accumulation of sand particles with increased share of solid phase around the centerline axis.

The same behavior can be detected from Fig. 14(a), which shows the time-mean contours of ε on a meridian cutting plane across the symmetry axis. For $d_R = 3$ and 5 cm, $\bar{\varepsilon}$ is at largest along the centerline axis due to the large-scale bubbles, which dominate the reactor volume. On the contrary, $\bar{\varepsilon}$ is lower at the centerline axis for the case with $d_R = 10$ cm, which indicates a higher concentration of sand particles there. This is attributed to the bubbles rising along multiple off-centered axes, resulting in a recirculation of the flow toward the centerline axis. For all cases, the time-averaged flow velocity $\bar{u}$ shown in Fig. 14(b) yields a positive correlation with $\bar{\varepsilon}$, which is small in the regions close to the wall and large in the core regions for $d_R = 3$ and 5 cm. For $d_R = 10$ cm, $\bar{u}$ is small in the core region due to recirculation of the flow or the particles toward the symmetry axis. The zones with the largest $\bar{\varepsilon}$ or $\bar{u}$ can be traced back to the rising bubbles.

Figure 15 shows the temporal developments of the specific kinetic energy of sand k_S calculated by using different reactor diameters. The table on the right summarizes the calculated time-mean bed height h_B (distance along the centerline axis from the reactor base to the position with $\bar{\varepsilon} = 0.99$), pressure drop Δp, $\bar{k}_S$, and bubble frequency f_B. h_B is slightly decreased with increased d_R, which can also be detected from the contour plots of ε shown in Fig. 14(a). In accordance with Eq. (13), the decrease in h_B with d_R leads to a slight decrease in Δp. The same behavior is found for $\bar{k}_S$, which is insensitive to the reactor size. As

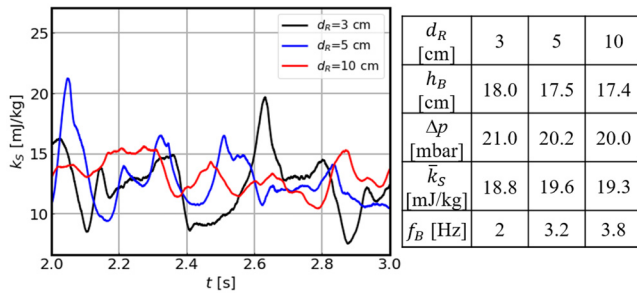| d_R [cm]	3	5	10
h_B [cm]	18.0	17.5	17.4
Δp [mbar]	21.0	20.2	20.0
$\overline{k}_S$ [mJ/kg]	18.8	19.6	19.3
f_B [Hz]	2	3.2	3.8

FIG. 15. Comparison of time evolution of specific kinetic energy (left) and list of calculated time-averaged bed height, pressure drop, specific kinetic energy, and bubble frequency (right) at up-scaled reactor dimension.

shown in Fig. 15, although k_S fluctuates in time at different d_R, the time-averaged values of k_S remain almost constant. However, the enhanced bubble formation at increased d_R has led to a clear increase in the bubble frequency. At larger reactor diameters, the occurrence of bubble chains accompanies with the development of the large-scale solid circulation, where the bubbles rise in close succession at high speed, leading to an increase in f_B. The results indicate that the kinetic energy or the averaged moving velocity of the sand particles remain almost constant while up-scaling the fluidized bed reactor. The dominant timescale with regard to the rising bubbles and the circulating bed materials is, however, decreased.

In summary, similar to the bed height h_B and pressure drop Δp, the specific kinetic energy k_S and the bubble frequency f_B represent integral properties of fluidized beds, which depend on the operating conditions or the dimensionless parameters like u_G* or Re. Compared with h_B and Δp, k_S and f_B can be used for a more detailed assessment of fluidized beds, which reveal dynamic behaviors of the particles and the bubbles in terms of their moving velocities. It has been shown in this work that, in the bubbling fluidization regime, k_S increases with the superficial velocity u_G due to the increased momentum flux of the gas flow and it increases with the operating temperature T_G due to the increased drag force, corresponding to a more intensive mixing or heating; on the contrary, Δp remains almost constant with u_G. In addition, f_B increases while up-scaling the fluidized bed, whereas h_B and Δp remain unaffected. These highlight the need of introducing additional performance-related parameters like k_S and f_B.

V. CONCLUSION

A laboratory-scale, cylindrical fluidized bed reactor has been studied numerically in cold-mode operation. The objective of this work is to assess the dynamic characteristics of the fluidized bed in terms of the total kinetic energy of the bed materials k_S and the bubble frequency f_B, which represent measures for the efficiency of multiphase momentum transfer and the dominant time scales prevailing the gas–solid system. The main findings are summarized below:

- The bubbling fluidization regime of the fluidized bed observed in experiments has been reproduced well by the simulations, where the calculated pressure drop has shown a good agreement with measured data.

- While varying the superficial flow velocity u_G and the bed inventory for a fixed geometry of the fluidized bed, k_S has found to increase with u_G. This is due to the increased momentum flux of the gas flow, leading to an enhanced aerodynamic forces exerted on the particles. The same behavior has been confirmed for the correlation of k_S with m_S.
- f_B decreases with m_S at constant u_G, which is attributed to the increased bed volume with m_S.
- At constant m_S and u_G, k_S increases with the reactor temperature T_G. This is caused by the increased kinetic viscosity of the gas, which leads to an increased drag force or enhanced gas-to-solid momentum transfer.
- An increase of the bed inventory via up-scaling results in enhanced formation of bubbles and an increased f_B. However, the averaged moving speed of the bed materials in terms of k_S, as well as the pressure drop and bed height remain almost unchanged.

The results reveal strong correlations of k_S and f_B with the operating parameters, which can be used to characterize the hydrodynamic behavior of fluidized beds. In particular, the commonly used properties such as Δp and h_B are not sufficient for studying effects related to scale-up or elevated temperature, as Δp and h_B are not sensitive to these conditions. In these cases, the proposed dynamic properties k_S and f_B represent suitable measures for a detailed assessment of the flow behaviors in fluidized beds.

AUTHOR DECLARATIONS
Conflict of Interest

The authors have no conflicts to disclose.

Author Contributions

Feichi Zhang: Conceptualization (lead); Investigation (lead); Methodology (lead); Supervision (equal); Writing – original draft (lead); Writing – review & editing (lead). **Dieter Stapf:** Conceptualization (equal); Funding acquisition (equal); Investigation (equal); Methodology (equal); Project administration (equal); Resources (equal); Supervision (equal). **Salar Tavakkol:** Conceptualization (supporting); Investigation (supporting); Project administration (equal); Supervision (supporting). **Stefan Dercho:** Methodology (equal); Software (equal); Visualization (equal). **Jialing Zhou:** Investigation (equal); Validation (lead); Visualization (lead). **Thorsten Zirwes:** Methodology (equal); Software (equal); Writing – review & editing (equal). **Michael Zeller:** Investigation (equal); Resources (equal); Writing – review & editing (equal). **Jonas Vogt:** Methodology (equal); Resources (equal); Writing – review & editing (equal). **Rui Zhang:** Supervision (equal). **Henning Bockhorn:** Supervision (equal).

DATA AVAILABILITY

The data that support the findings of this study are available from the corresponding author upon reasonable request.

REFERENCES

[1]J. Davidson and D. Harrison, *Fluidization* (Academic Press, London, 1971).

[2]D. Kunii and O. Levenspiel, *Fluidization Engineering* (John Wiley & Sons, New York, 1991).

[3]Z. Wan, S. Yang, and H. Wang, "MP-PIC investigation of the multi-scale gas–solid flow in the bubbling fluidized bed," Exp. Comput. Multiphase Flow **3**, 289–302 (2021).

[4]S. Elghobashi, "On predicting particle-laden turbulent flows," Appl. Sci. Res. **52**, 309–329 (1994).

[5]D. Gidaspow, *Multiphase Flow and Fluidization: Continuum and Kinetic Theory Description* (Academic Press, 1994).

[6]J. Grace and G. Sun, "Influence of particle size distribution on the performance of fluidized bed reactors," Can. J. Chem. Eng. **69**, 1126–1134 (1991).

[7]H. R. Norouzi, R. Zarghami, R. Sotudeh-Gharebagh, and N. Mostoufi, *Coupled CFD-DEM Modeling* (John Wiley & Sons, 2016), Vol. 91.

[8]N. Deen, M. Van Sint Annaland, M. Van der Hoef, and J. Kuipers, "Review of discrete particle modeling of fluidized beds," Chem. Eng. Sci. **62**, 28–44 (2007).

[9]F. Alobaid, N. Almohammed, M. M. Farid, J. May, P. Rößger, A. Richter, and B. Epple, "Progress in CFD simulations of fluidized beds for chemical and energy process engineering," Prog. Energy Combust. Sci. **91**, 100930 (2022).

[10]Q. Wang, H. Yang, P. Wang, J. Lu, Q. Liu, H. Zhang, L. Wei, and M. Zhang, "Application of CPFD method in the simulation of a circulating fluidized bed with a loop seal, part I–Determination of modeling parameters," Powder Technol. **253**, 814–821 (2014).

[11]Q. Wang, H. Yang, P. Wang, J. Lu, Q. Liu, H. Zhang, L. Wei, and M. Zhang, "Application of CPFD method in the simulation of a circulating fluidized bed with a loop seal part II–Investigation of solids circulation," Powder Technol. **253**, 822–828 (2014).

[12]D. Gündüz Raheem, B. Y. ilmaz, and S. Özdoğan, "Cold flow simulation of a 30 kWth CFB riser with CPFD," J. Appl. Fluid Mech. **13**, 603–614 (2020).

[13]F. Zafiryadis, A. D. Jensen, Y. Laxminarayan, W. Lin, M. B. Larsen, E. A. Hove, and H. Wu, "Predicting cold gas-solid flow in a pilot-scale dual-circulating fluidized bed: Validation of computational particle fluid dynamics model," Powder Technol. **381**, 25–43 (2021).

[14]A. Lunzer, S. Kraft, S. M, and H. Hofbauer, "CPFD simulation of a dual fluidized bed cold flow model," Biomass Convers. Biorefin. **11**, 189–203 (2021).

[15]Q. Wu, S. Wang, K. Zhang, Y. Zhao, and Y. He, "Numerical studies of gas-solid flow behaviors and wall wear in a swirling fluidized bed," Powder Technol. **388**, 233–240 (2021).

[16]X. Liu, G. Niels, and Y. Tang, "On the treatment of bed-to-wall heat transfer in CFD-DEM simulations of gas-fluidized beds," Chem. Eng. Sci. **236**, 116492 (2021).

[17]Q. Tu, H. Wang, and R. Ocone, "Application of three-dimensional full-loop CFD simulation in circulating fluidized bed combustion reactors—A review," Powder Technol. **399**, 117181 (2022).

[18]S. Tenneti, "Particle-resolved direct numerical simulation for gas-solid flow model development," Annu. Rev. Fluid Mech. **46**, 199–230 (2014).

[19]M. Moriche, D. Hettmann, M. García-Villalba, and M. Uhlmann, "On the clustering of low-aspect-ratio oblate spheroids settling in ambient fluid," J. Fluid Mech. **963**, A1 (2023).

[20]S. Tenneti, M. Mehrabadi, and S. Subramaniam, "Stochastic Lagrangian model for hydrodynamic acceleration of inertial particles in gas–solid suspensions," J. Fluid Mech. **788**, 695–729 (2016).

[21]A. Esteghamatian, A. Hammouti, M. Lance, and A. Wachs, "Particle resolved simulations of liquid/solid and gas/solid fluidized beds," Phys. Fluids **29**(3), 033302 (2017).

[22]D. Domínguez-Vázquez, G. B. Jacobs, and D. M. Tartakovsky, "Lagrangian models of particle-laden flows with stochastic forcing: Monte Carlo, moment equations, and method of distributions analyses," Phys. Fluids **33**(3), 033326 (2021).

[23]D. Domínguez-Vázquez, B. F. Klose, and G. B. Jacobs, "Closed SPARSE—a predictive particle cloud tracer," Int. J. Multiphase Flow **161**, 104375 (2023).

[24]A. M. Lattanzi, V. Tavanashad, S. Subramaniam, and J. Capecelatro, "Stochastic models for capturing dispersion in particle-laden flows," J. Fluid Mech. **903**, A7 (2020).

[25]A. M. Lattanzi, V. Tavanashad, S. Subramaniam, and J. Capecelatro, "Stochastic model for the hydrodynamic force in Euler–Lagrange simulations of particle-laden flows," Phys. Rev. Fluids **7**(1), 014301 (2022).

[26]S. Balachandar and K. Liu, "A correction procedure for self-induced velocity of a finite-sized particle in two-way coupled Euler–Lagrange simulations," Int. J. Multiphase Flow **159**, 104316 (2023).

[27]J. A. K. Horwitz, G. Iaccarino, J. K. Eaton, and A. Mani, "The discrete green's function paradigm for two-way coupled Euler–Lagrange simulation," J. Fluid Mech. **931**, A3 (2022).

[28]D. Domínguez-Vázquez and G. B. Jacobs, "SPARSE–R: A point-cloud tracer with random forcing," Int. J. Multiphase Flow **170**, 104653 (2024).

[29]R. G. Patel, O. Desjardins, B. Kong, J. Capecelatro, and R. O. Fox, "Verification of Eulerian–Eulerian and Eulerian–Lagrangian simulations for turbulent fluid–particle flows," AIChE J. **63**(12), 5396–5412 (2017).

[30]F. Evrard, F. Denner, and B. van Wachem, "Euler–Lagrange modelling of dilute particle-laden flows with arbitrary particle-size to mesh-spacing ratio," J. Comput. Phys. **8**, 100078 (2020).

[31]J. Capecelatro and O. Desjardins, "An Euler–Lagrange strategy for simulating particle-laden flows," J. Comput. Phys. **238**, 1–31 (2013).

[32]M. Kuerten, "Point-particle DNS and LES of particle-laden turbulent flow—a state-of-the-art review," Flow, Turbul. Combust. **97**, 689–713 (2016).

[33]C. Loha, S. Gu, J. Wilde, P. Mahanta, and P. Chatterjee, "Advances in mathematical modeling of fluidized bed gasification," Renewable Sustainable Energy Rev. **40**, 688–715 (2014).

[34]S. Harris and D. Crighton, "Solitons solitary waves, and voidage disturbances in gas-fluidized beds," J. Fluid Mech. **266**, 243 (1994).

[35]D. Snider, "An incompressible three-dimensional multiphase particle-in-cell model for dense particle flows," J. Comput. Phys. **170**, 523–549 (2001).

[36]V. Baranau and U. Tallarek, "Random-close packing limits for monodisperse and polydisperse hard spheres," Soft Matter **10**, 3826–3841 (2014).

[37]P. O'Rourke and D. Snider, "Inclusion of collisional return-to-isotropy in the MP-PIC method," Chem. Eng. Sci. **80**, 39–54 (2012).

[38]J. R. Grace, "Contacting modes and behaviour classification of gas–solid and other two–phase suspensions," Can. J. Chem. Eng. **64**(3), 353–363 (1986).

[39]J. Schmid, T. Pröll, H. Kitzler, C. Pfeiffer, and H. Hofbauer, "Cold flow model investigations of the countercurrent flow of a dual circulating fluidized bed gasifier," Biomass Convers. Biorefin. **2**, 229–244 (2012).

[40]H. T. Bi and J. R. Grace, "Flow regime diagrams for gas-solid fluidization and upward transport," Int. J. Multiphase Flow **21**(6), 1229–1236 (1995).

[41]See https://www.openfoam.com/news/main-news/openfoam-v2112 for OpenFOAM, OpenCFD Release OpenFOAM v2112.

[42]E. Michaelides, C. Crowe, and J. Schwarzkopf, *Multiphase Flow Handbook* (CRC Press, Boca Raton, 2016).

[43]J. Werther, "Numerical studies of gas–solid flow behaviors and wall wear in a swirling fluidized bed," Chem.-Ing. Tech. **54**, 876–883 (1982).

[44]M. Zeller, N. Netsch, F. Richter, H. Leibold, and D. Stapf, "Chemical recycling of mixed plastic wastes by pyrolysis–pilot scale investigations," Chem. Ing. Tech. **93**, 1763–1770 (2021).